Molecular interactions at the metal-liquid interfaces

Mathilde Orselly, Julien Devémy, Agathe Bouvet-Marchand, Alain Dequidt, Cedric Loubat, Patrice Malfreyt

Molecular interactions at the metal-liquid interfaces

Mathilde Orselly,[1, 2, a)] Julien Devémy,[2] Agathe Bouvet-Marchand,[1] Alain Dequidt,[2] Cédric Loubat,[1] and Patrice Malfreyt[2, b)]

[1)] *Specific Polymers, 150 Avenue des Cocardières, 34160, Castries, France*

[2)] *Université Clermont Auvergne, CNRS, Clermont Auvergne INP, Institut de Chimie de Clermont-Ferrand, F-63000 Clermont-Ferrand, France*

(Dated: 20 May 2022)

We reported molecular simulations of the interactions between water, an epoxy prepolymer (DGEBA) and an hardener (IPDA) on an aluminum surface. This work proposes a comprehensive thermodynamic characterization of the adhesion process from the calculation of the different interfacial tensions. The cross-interactions between the atoms of the metal surface and the different molecules are adjusted so as to reproduce the experimental work of adhesion. Water nanodroplets on the metal surface are then simulated to predict its contact angle. Liquid-vapor surface tensions of the epoxy prepolymer (DGEBA) and hardener (IPDA) and the solid-vapor surface tension of the aluminum surface are also calculated to provide the solid-liquid interfacial tension that remains very difficult to obtain from the mechanical definition.

I. INTRODUCTION

Understanding the behavior of a fluid in the vicinity of a surface is fundamental for many disciplines such as chemistry, physics, biology and medicine. It involves a macroscopic characterization of the phenomena at the interface and a complete description of the microscopic arrangements in the interfacial region. The knowledge of these interfacial interactions and structures is key to many applications involving adsorption, wetting properties of a surface, biocompatibility of a material and polymer materials such as nanocomposites and membranes.

To energetically characterize the affinity of a liquid for a surface, experiments usually measure the Young contact angle θ, which is related to different surface tensions through the Young's equation[1–3].

$$\gamma_{\mathrm{SL}} - \gamma_{\mathrm{SV}} + \gamma_{\mathrm{LV}} \cos\theta = 0 \tag{1}$$

where γ_{SL}, γ_{SV} and γ_{LV} are the solid-liquid, solid-vapor and liquid-vapor surface tensions, respectively. For contact angle values less than 90°, the liquid spreading over a large area on the solid surface, indicates that the wetting of the solid surface is favorable. The wetting is complete for $\theta = 0°$. For contact angles greater than 90°, the liquid tries to minimize its contact with the surface by forming a compact liquid drop.

A related but key property is the work of adhesion W_{SL} per unit of area of the solid-liquid interface. This property can be defined as the reversible thermodynamic work needed to separate the solid-liquid interface from the equilibrium state of two coexisting phases to a separation distance of infinity[4].

$$W_{\mathrm{SL}} = \gamma_{\mathrm{LV}} + \gamma_{\mathrm{SV}} - \gamma_{\mathrm{SL}} \tag{2}$$

Using Eq.(1), the work of adhesion can also be obtained in terms of the contact angle such as

$$W_{\mathrm{SL}} = \gamma_{\mathrm{LV}} \left(1 + \cos\theta\right) \tag{3}$$

For positive values of W_{SL}, we deduce that the higher the value of W_{SL} is, the stronger the interaction between the solid and the liquid components are. Indeed, for optimum adhesion, W_{SL} must be maximized which occurs when the solid-liquid interfacial tension γ_{SL} approaches zero (Eq.(2)).

Molecular simulations[5,6] have opened up important theoretical and methodological fields of investigation on interfacial systems with the aim of describing the interface and predicting surface tension. The link between the atomistic models and the surface tension is made through the statistical mechanics of inhomogeneous systems[7]. The first simulation was carried out in the 1970s and focused on the liquid-vapor interface of a Lennard-Jones fluid[8,9]. Many debates have animated this research activity because simulation results have suffered from many dependencies to input parameters. It took almost 50 years to solve all the methodological problems due to the modeling of an interface, namely the impact of the truncation of the potential[10–12], the importance of the long range corrections to the surface tension[13], the calculation of the surface tension through the mechanical and thermodynamic definition[14] and size-effects[15]. In conclusion, the calculation of surface tension is now under control in the case of liquid-vapor and liquid-liquid interfaces[5].

The same cannot be said for the calculation of the interfacial tension between a solid and a fluid[6]. Indeed, the interfacial thermodynamics in the solid-liquid and solid-vapor interfaces is different from that of liquid-liquid and liquid-vapor interfaces. The calculation of the solid-liquid (γ_{SL}) and solid-vapor (γ_{SV}) is much more sophisticated, since it must consider the internal stress in the solid phase. The relationship between the surface tension and the surface stress tensor $\sigma_{\alpha\beta}$, first given by

[a)] Electronic mail: Mathilde.Orselly@specificpolymers.fr

[b)] Electronic mail: Patrice.Malfreyt@uca.fr

Shuttleworth[16], is

$$\sigma_{\alpha\beta} = \gamma_{\mathrm{SL}}\,\delta_{\alpha\beta} + A\,\frac{\partial \gamma_{\mathrm{SL}}}{\partial \epsilon_{\alpha\beta}} \tag{4}$$

where A is the cross-sectional area, $\epsilon_{\alpha\beta}$ the $\alpha\beta$ component of the elastic strain tensor[17]and $\delta_{\alpha\beta}$ the Kronecker delta. For interfacial systems involving only fluids, the second term in Eq.(4) is considered null, and the surface tension is obtained from the stress profile. For solid-liquid interfaces, other alternatives have been developed to avoid the calculation of the elastic strain tensor. Capillary-wave oscillations can be used to estimate the solid-liquid interfacial energy[18]. The phantom-wall methodology[19–22] consists of using the thermodynamic integration method to calculate the Gibbs interfacial excess free energy between a solid-liquid interface and an unstructured phantom surface. The test-area method has also been applied to the calculation of the solid-liquid interfacial tension[23]. Another route[24] referred to as the cleaving method, consists of calculating the free energy required to create the solid-liquid interface from the separated bulk phases. This technique has been applied to the crystal-melt interfacial free energy[24].

Nevertheless, under facilitating conditions, the calculation of γ_{SL} can be conducted by using the pressure tensor definition. In this case, a rigid surface with no intramolecular interactions is considered. The configuration of the atoms of the surface is not changed and no internal stresses are generated. We have performed this type of calculation on a sheet of graphene which is isotropic by nature. In this case, γ_{SL} can be calculated in the same way as it is calculated in fluid-fluid interfaces. We have recently used this approach for the calculation of the solid-liquid interfacial tension in the graphene-liquids interface[25–29]. We have shown that the simulated graphene-water interfacial tension[27] was in line with that obtained from experiments[30]. For more complex surfaces, such as metallic ones, this mechanical approach can no longer be used.

In this paper, we aim to investigate the interfacial tensions that contribute to the energy balance of the adhesion between a solid and a fluid. We mainly focus on the adhesion of the components of epoxy resins onto metal surfaces. These systems are relevant for industrial processes due to the prominence of epoxies for a wide range of applications[31]. These thermosetting polymers can be used for structural components in aerospace applications or as various types of coatings. The adhesion between the substrate and the polymer is thus an undeniable aspect of the success of the resulting material, and its characterization is crucial.

To do so, we tackled the calculation of the work of adhesion of different metal-fluids interfaces by using the concept of Free Energy Perturbation (FEP)[32–35]. This approach has been recently applied to the case of the interaction between a graphene sheet and water[21,36]. We also applied this approach to evaluate the solid-vapor interfacial tension of metal surfaces. From the calculation of the liquid-vapor surface tension of components of resins, we proposed to determine the solid-liquid interfacial tension. We have measured the values of contact angle when they were not available in the literature. This study aims to show that it is possible to reproduce the work of adhesion of metal-fluid systems by playing on the cross-interactions.

The paper is organized as follows. Section II describes the simulation and experimental methods. Section III discusses the calculations of interfacial tensions of different systems. Section IV contains our conclusions.

II. EXPERIMENTAL AND SIMULATION METHODS

A. Description of the force field

The CHARMM General Force Field (CgenFF)[37–39] is used to describe the intra- and inter-molecular interactions of the thermosetting polymers. This Class I force field has the following functional form:

$$\begin{aligned}
\mathcal{U} = & \sum_{Bonds} k_r\,(r_{ij} - r_0)^2 \\
& + \sum_{Angles} k_\theta\,(\theta_{ijk} - \theta_0)^2 \\
& + \sum_{Dihedrals} \sum_{n} k_{\varphi,n}\,[1 + \cos(n\,\varphi_{ijkl} - \delta_n)] \\
& + \sum_{Impropers} k_\phi\,(\phi_0 - \phi_0)^2 \\
& + \sum_{Urey-Bradley} k_{ub}\,(r_{1,3} - r_{1,3_0})^2 \\
& + \sum_{Nonbonded\ atoms} S(r_{ij})\,\frac{q_i\,q_j}{4\pi\,\epsilon_0\,r_{ij}} \\
& + \sum_{Nonbonded\ atoms} S(r_{ij})\,\varepsilon_{ij}\left[\left(\frac{R_{min,ij}}{r_{ij}}\right)^{12} - 2\left(\frac{R_{min,ij}}{r_{ij}}\right)^{6}\right]
\end{aligned} \tag{5}$$

The total potential energy $\mathcal{U}$ sums then the bond (r_{ij}), valence angle (θ), Urey-Bradley (r_{13}), dihedral angle (φ) and improper angle (ϕ) interactions and non-bonded interactions modelled by Lennard-Jones and Coulombic potentials. k_θ, $k_{\varphi,n}$, k_{ub}, k_ϕ are the force constants and the variables with the subscript 0 represent the equilibrium values. The parameter R_{min} used in the Lennard-Jones potential corresponds to $2^{1/6}\sigma$ where σ is the atomic diameter. The CHARMM force field presents an additional component in the form of the Urey-Bradley term, which consists of a harmonic potential as a function of the distance between the non-bonded atoms 1 and 3 of an 1-2-3 angle.

The Lennard-Jones parameters between pairs of different atoms are obtained from the Lorentz-Berthelot combination rules, in which ε_{ij} values are calculated by using the geometric mean and R_{min} values uses the arithmetic

mean. The cut-off distance for van der Waals interactions is set to $r_{c1} = 8.0\,\text{Å}$ while the Particle-Particle Particle Mesh (PPPM) method with an accuracy of 1.0×10^{-4} and a cut-off of 8 Å is considered for the long-range electrostatic interactions. For both the Lennard-Jones and Coulombic interactions, a force-switching function was applied between $r_{c1} = 8\,\text{Å}$ and $r_{c2} = 10\,\text{Å}$. The $S(r_{ij})$ function, defined as

$$S(r_{ij}) = \begin{cases} 1, & \text{if } r_{ij} \leq r_{c1} \\ \frac{(r_{c2}^2 - r_{ij})^2\,(r_{c2}^2 + 2\,r_{ij}^2 - 3\,r_{c1}^2)}{(r_{c2}^2 - r_{c1}^2)^3}, & \text{if } r_{c1} < r_{ij} \leq r_{c2} \end{cases} \tag{6}$$

yields a continuous potential energy and force at the cut-off radii r_{c1} and r_{c2}.

The Velocity-Verlet integrator was used to integrate the equations of motion using a time step of 1 fs. The SHAKE algorithm was applied to constrain the length of covalent bonds to hydrogen atoms to their equilibrium values. In order to control the temperature and pressure for NVT and NPT simulations, a Nosé-Hoover thermostat and barostat were applied[40]. Unless stated otherwise, the MD simulations were performed at 300 K and 1 atm. The molecular dynamics (MD) calculations were performed using the LAMMPS package[41].

Aluminum was created by using the *Atomsk* software[42]. A repetition of the elementary mesh in the three directions of space XYZ was then possible. This makes it feasible to create a metal block for atomistic simulations based on the structure of the latter and its lattice parameters. It was chosen to investigate the {100} planes of this face-centered cubic crystal. The lattice parameters of aluminum is 4.0496 Å.[43] Regarding the force field[44] associated with these types of atoms, metals are only linked together by non-covalent bonds, known as metallic bonds. In these simulations, each metallic atom is considered neutral. Lennard-Jones interactions are employed to maintain the system at equilibrium. For the aluminum surface, the parameters developed in Ref. 44 are transformed to fit the equations of the CHARMM force field as in Table I.

TABLE I. Parameters from the CHARMM force field[44] for the aluminum atoms

Metals	Mass (g)	σ (Å)	ε (kJ mol^{-1})
Al	26.98	2.6059	16.83

Various molecules were modelled in order to estimate the influence of the chemical structure on the interface. In the framework of this study, the following molecules were used : DGEBA (diglycidic ether of bisphenol A) and IPDA (isophorone diamine) (see Figures 1a and 1b). The force field of the molecules does not differ and is also based on the CHARMM General Force Field. The water molecules were modelled by using the flexible version of the SPC water model[45].

B. Calculation of the work of adhesion W_{SL}

In a classical system constituted by N identical particles of mass m defined by their coordinates $\mathbf{r}^N$ and momenta $\mathbf{p}^N$, the Helmholtz free energy F is related to the partition function Q_{NVT} in the constant-NVT ensemble by the following expression

$$\begin{aligned} F &= -\frac{1}{\beta}\ln Q_{\text{NVT}} \\ &= -\frac{1}{\beta}\ln\left(\frac{1}{h^{3N}N!}\int\int d\mathbf{r}^N d\mathbf{p}^N \exp\left(-\beta\,\mathcal{H}(\mathbf{r}^N,\mathbf{p}^N)\right)\right) \\ &= -\frac{1}{\beta}\ln\left(\frac{1}{\Lambda^{3N}N!}\int d\mathbf{r}^N \exp\left(-\beta\,\mathcal{U}(\mathbf{r}^N)\right)\right) \end{aligned} \tag{7}$$

where $\beta = \frac{1}{k_B T}$ is the inverse temperature and h the Planck constant. The total Hamiltonian in Eq.(7) can be written as the sum of the kinetic and potential energies of the system. Let us suppose that the potential energy $\mathcal{U}(\mathbf{r}^N)$ is independent of the velocities, the double integral in Eq.(7) can be separated in two integrals, one over the positions and one over the momenta. This latter can be written in terms of the de Broglie thermal wavelength, Λ. The resulting expression of the Helmholtz free energy is given by Eq.(8).

$$\begin{aligned} \Delta F = F^{(1)} - F^{(0)} &= -\frac{1}{\beta}\ln\frac{Q^{(1)}_{\text{NVT}}}{Q^{(0)}_{\text{NVT}}} \\ &= -\frac{1}{\beta}\ln\left\langle \exp\left[-\beta\left(\mathcal{H}^{(1)}(\mathbf{r}^N,\mathbf{p}^N) - \mathcal{H}^{(0)}(\mathbf{r}^N,\mathbf{p}^N)\right)\right]\right\rangle_{(0)} \end{aligned} \tag{8}$$

where $\mathcal{H}^{(1)}(\mathbf{r}^N,\mathbf{p}^N)$ and $\mathcal{H}^{(0)}(\mathbf{r}^N,\mathbf{p}^N)$ are the total Hamiltonian of the target and reference systems, respectively. The expression of Eq.(8) is the fundamental expression of the Free Energy Perturbation (FEP)[32–35] methodology. The reference system denoted as (0) is defined by the interaction between the solid and liquid phases characterized by γ_{SL}. The target system (1) is then formed by a solid phase and a liquid phase in equilibrium with their vapor. Both phases no longer interact with each other and lead to two interfacial tensions γ_{LV} and γ_{SV}. We can describe the transformation with the following expression:

$$\Delta F = \mathcal{A}\,W_{\text{SL}} = \mathcal{A}\sum_{i=1}^{N_w-1} W_{\text{SL}}(\lambda_i) = \mathcal{A}\left(\gamma_{\text{LV}} + \gamma_{\text{SV}} - \gamma_{\text{SL}}\right) \tag{9}$$

where $\mathcal{A}$ is the surface area of the solid. Since the transformation does not involve any changes in terms of mass and temperature, it results that the kinetic term obtained through the de Broglie thermal wavelength cancels out. As a consequence, we replace the Hamiltonian by the potential energy $\mathcal{U}(\mathbf{r}^N)$ and we will omit the dependence of $\mathcal{U}$ on the positions $\mathbf{r}^N$ for simplicity of notation.

To improve the convergence of the calculation and to promote overlaps between consecutive steps, the calculation of the free energy difference ΔF between two states (0) and (1) is split into N_w intermediate contiguous states or windows defined by a coupling constant λ_i. The potential energy is a function of λ_i as described by Eq.(10)

$$\mathcal{U}(\lambda_i) = \lambda_i \mathcal{U}(\lambda_{N_w}) + (1-\lambda_i)\mathcal{U}(\lambda_1) \tag{10}$$

where $0 \leq \lambda_i \leq 1$, $\lambda_1 = 0$ and $\lambda_{N_w} = 1$. Eq.(7) can be rewritten in the context of the calculation over consecutive states (i) and $(i+1)$ by

$$\begin{aligned}
\Delta F &= F^{(1)} - F^{(0)} = \sum_{i=1}^{N_w-1} \Delta F(\lambda_i) \\
&= -\frac{1}{\beta}\sum_{i=1}^{N_w-1} \ln \left\langle \exp\left[-\beta\Big(\mathcal{U}(\lambda_{i+1}) - \mathcal{U}(\lambda_i)\Big)\right]\right\rangle_{\lambda_i} \quad (11)\\
&= +\frac{1}{\beta}\sum_{i=2}^{N_w} \ln \left\langle \exp\left[-\beta\Big(\mathcal{U}(\lambda_{i-1}) - \mathcal{U}(\lambda_i)\Big)\right]\right\rangle_{\lambda_i} \quad (12)
\end{aligned}$$

The perturbations can be performed in both directions ("double-wide sampling") with N_w windows over the entire simulation. In principle, for a reversible process, ΔF calculated in the forward direction with Eq.(11) and backward direction with Eq.(12) should be equal. The difference between the forward ($\Delta\lambda = \lambda_{i+1} - \lambda_i$) and backward ($\Delta\lambda = \lambda_{i-1} - \lambda_i$) simulations gives a lower-bound estimate of the error in the calculations. The transformation from state (i) to state $(i+1)$ is achieved by changing the interactions between the solid and the liquid molecules and keeping identical the solid-solid and liquid-liquid interactions. This is done by applying the following rules to the cross interactions between the atoms of the solid and liquid phases, such as

$$\varepsilon_{SL}(\lambda_i) = (1-\lambda_i)\sqrt{\varepsilon_{SS}\varepsilon_{LL}} \tag{13}$$

where S and L represent atoms of the solid and liquid phases, respectively.

The removal of the interactions between the solid and liquid atoms (see Figure 1c) can lead to instabilities when the coupling parameter λ_i approaches 0. A solution[46] is to modify the Lennard-Jones potential as

$$U_{\mathrm{LJ}}(r_{ij},\lambda_i) = (1-\lambda_i)\,\varepsilon_{ij}\left[\frac{1}{\left(\mu\,(\lambda_i)^2 + \left(\frac{R_{min,ij}}{r_{ij}}\right)^6\right)^2} - \frac{1}{\mu\,(\lambda_i)^2 + \left(\frac{R_{min,ij}}{r_{ij}}\right)^6}\right] \tag{14}$$

where μ was taken to 0.5. As λ_i is 0, the solid and liquid molecules interact through the full strength of the Lennard-Jones potential. As λ_i approaches 1, the Lennard-Jones potential is modified by a soft-core interaction $\mu\,\lambda_i^2$.

C. Calculation of the surface tension

1. Mechanical definition

The surface tension γ, originally given by Kirkwood and Buff[47], is defined by

$$\gamma = \frac{1}{2}\left\langle p_{\mathrm{N}} - p_{\mathrm{T}} \right\rangle L_z \tag{15}$$

where p_{N} and p_{T} are the normal and tangential components of the pressure and L_z is the length of the simulation cell in the z direction. Since a two phase simulation (see Figure 1d) with periodic boundary conditions consists of two interfaces, the surface tensions calculated from Eq.(15) is divided by 2 to calculate γ for a single interface. For a planar interface, p_{N} is given by p_{zz}, whereas the tangential component p_T is given by $\frac{1}{2}(p_{xx} + p_{yy})$.

Irving and Kirkwood[7,47–51] have shown that γ can be calculated from $p_{\mathrm{N}}(z)$ and $p_{\mathrm{T}}(z)$, the components of the pressure tensor as a function of z;

$$\gamma = \frac{1}{2}\int_{-L_z/2}^{L_z/2} \left(p_{\mathrm{N}}(z) - p_{\mathrm{T}}(z)\right) dz \tag{16}$$

This local definition of γ, based on the mechanical road, uses the force acting across a unit area in the z-plane for one interface. There is no unique way of calculating the forces across a particular area, since it is unclear which atoms contribute to this force. This has no effect on $p_{\mathrm{N}}(z)$ but different choices of the contour can affect the definition of $p_{\mathrm{T}}(z)$. However, these choices have no effect on the integral in Eq.(16). We use here the Harasima definition[7,47,52] for the normal and tangential pressure components. The normal component of the pressure tensor can be written as

$$\begin{aligned}
p_{\mathrm{N}}(z) &= \langle\rho(z)\rangle\, k_B T \\
&+ \frac{1}{2\,\mathcal{A}\,\Delta z}\left\langle \sum_{i=1}^{N-1}\sum_{j=i+1}^{N}\Big(z_{ij}\,(\mathbf{f}_{ij})_z\Big) \right. \\
&\times \left. \left(\delta(z-z_i) + \delta(z-z_j)\right)\right\rangle
\end{aligned} \tag{17}$$

where $\mathcal{A}$ is the surface area, Δz is the thickness of the slab and $\rho(z)$ is the local number density. The simulation box is divided into N_z slabs of thickness δz. $\mathbf{f}_{ij}$ is the force between atoms i and j defined as:

$$\mathbf{f}_{ij} = -\frac{\mathbf{r}_{ij}}{r_{ij}}\,\frac{d\mathcal{U}(r_{ij})}{dr_{ij}} \tag{18}$$

where $\mathcal{U}$ represents all the intramolecular and intermolecular energy contributions described in the force field of Eq.(5). The tangential component of the pressure tensor is then expressed as follows

$$\begin{aligned} p_{\mathrm{T}}(z) &= \langle \rho(z) \rangle \, k_B T \\ &+ \frac{1}{4\,\mathcal{A}\,\Delta z} \Bigg\langle \sum_{i=1}^{N-1} \sum_{j=i+1}^{N} \Big(x_{ij} \left(\mathbf{f}_{ij}\right)_x + y_{ij} \left(\mathbf{f}_{ij}\right)_y \Big) \\ &\times \left(\delta(z - z_i) + \delta(z - z_j)\right) \Bigg\rangle \end{aligned} \tag{19}$$

These equations indicate that half of the virial contributions arising between atom i and atom j is assigned to the slab where i is located and the other half to the slab where j is located. Since intermolecular energies and forces are modified by a switching function that makes energy and forces equations decrease smoothly to zero at the cutoff, no long-range corrections due to the truncated potentials need to be applied to the pressure components and surface tension.

2. Calculation of the solid-vapor surface γ_{SV}

In order to obtain the solid-vapor surface tension, a methodology based on the difference of average total energy is used between two NVT simulations[44]. Two boxes are utilized : a split box with two slabs of metal separated by vacuum, and a unified box grouping these two slabs together. Both simulations cells have the same dimensions and the same total number of atoms. The difference in total energy between the separated structure (E_{S}) and the unified structure (E_{U}) corresponds to the cleavage energy per surface area. Two solid-vapor interfaces have been created during the cleavage process. This definition is based on the calculation of the energy and therefore neglects the entropy variations by considering that these contributions are negligible compared to the cohesive energy contribution, which is a fair approximation for metals at room temperature. The surface tension γ_{SV} is then defined as

$$\gamma_{\mathrm{SV}} = \frac{E_{\mathrm{S}} - E_{\mathrm{U}}}{2\,\mathcal{A}} - T\,\frac{S_{\mathrm{S}} - S_{\mathrm{U}}}{2\,\mathcal{A}} \approx \frac{E_{\mathrm{S}} - E_{\mathrm{U}}}{2\,\mathcal{A}}. \tag{20}$$

It is also possible to extend the calculation of W_{SL} to W_{SV} by adapting Eq.(9) to the solid-vapor interface. In this case, by using the Free Energy Perturbation, Eq.(9) becomes

$$\begin{aligned} \Delta F = \mathcal{A}\, W_{\mathrm{SV}} &= \mathcal{A} \sum_{i=1}^{N_w - 1} W_{\mathrm{SV}}(\lambda_i) \\ &= \mathcal{A}\,(2\,\gamma_{\mathrm{SV}} - \gamma_{\mathrm{SS}}) = 2\,\mathcal{A}\,\gamma_{\mathrm{SV}} \end{aligned} \tag{21}$$

where $\gamma_{\mathrm{SS}} = 0$ due to the energy/entropy compensation in the solid phase. By definition, this approach has the advantage of considering the entropic contribution. The initial state ($\lambda_1 = 0$) is defined by the two slabs of metal interacting with each other, and the final state ($\lambda_{N_w} = 1$) by two slabs of metal that no longer interact and are separated by vacuum. The perturbation consists in annihilating progressively the cross interactions between the atoms of both metal slabs. The vanishing of the interactions between the two groups of metal atoms is carried out through Eq.(22)

$$\varepsilon_{SV}(\lambda_i) = (1 - \lambda_i)\sqrt{\varepsilon_{(SS)_1}\varepsilon_{(SS)_2}} \tag{22}$$

where 1 and 2 refer to both groups of metal atoms.

During the transformation process, we can apply another methodology based on the concept of Thermodynamic Integration (TI)[35] for the calculation of the free energy. This TI definition allows a faster convergence and a smaller number of windows.

$$\begin{aligned} \Delta F &= \int_0^1 \left(\frac{\partial F}{\partial \lambda}\right) d\lambda = -\frac{1}{\beta} \int_0^1 \frac{1}{Q_{\mathrm{NVT}}} \left(\frac{\partial Q_{\mathrm{NVT}}}{\partial \lambda}\right) d\lambda \\ &= \int_0^1 \left\langle \frac{\partial \mathcal{U}}{\partial \lambda} \right\rangle_{\lambda_i} d\lambda \end{aligned} \tag{23}$$

with

$$\left\langle \frac{\partial \mathcal{U}}{\partial \lambda} \right\rangle_{\lambda_i} = \frac{\Big(\mathcal{U}(\lambda_{i+1}) - \mathcal{U}(\lambda_i)\Big)}{\delta\lambda} \tag{24}$$

and $\lambda_{i+1} = \lambda_i + \delta\lambda$ with $\delta\lambda = 2 \times 10^{-3}$. In practice, the change in the cross-interactions between solid atoms is done by changing $\lambda + \Delta\lambda$ by $\lambda + \delta\lambda$ in Eq.(22).

W_{SV} is the contribution calculated from $\lambda = 0$ to $\lambda = 1$ but the following contribution $W_{\mathrm{SV}}(\lambda)$ in Eq.(25) calculated on intermediate states from $\lambda = 0$ to λ, although not physically meaningful, allows to check the accuracy of the calculation at each steps and to compare the value with that calculated with FEP.

$$W_{\mathrm{SV}}(\lambda) = \int_0^{\lambda} \left\langle \frac{\partial \mathcal{U}}{\partial \lambda} \right\rangle_{\lambda_i} d\lambda \tag{25}$$

D. Experimental determination of the contact angle

Distilled water, DGEBA (diglycidic ether of bisphenol A) and IPDA (isophorone diamine) were used as contact angle measurement liquids on a 2024 aluminum alloy surface. The measurements were performed with an optical contact angle measuring system: OCA 50, DataPhysics Instruments GmbH. Measurements were made at room temperature (20 °C), except for DGEBA (70 °C) due to its viscosity. Sessile drop method was used to measure

the contact angle by a direct measurement of the tangent angle at the three-phase contact point. For each system, five drops of each liquid were tested on the metallic surface.

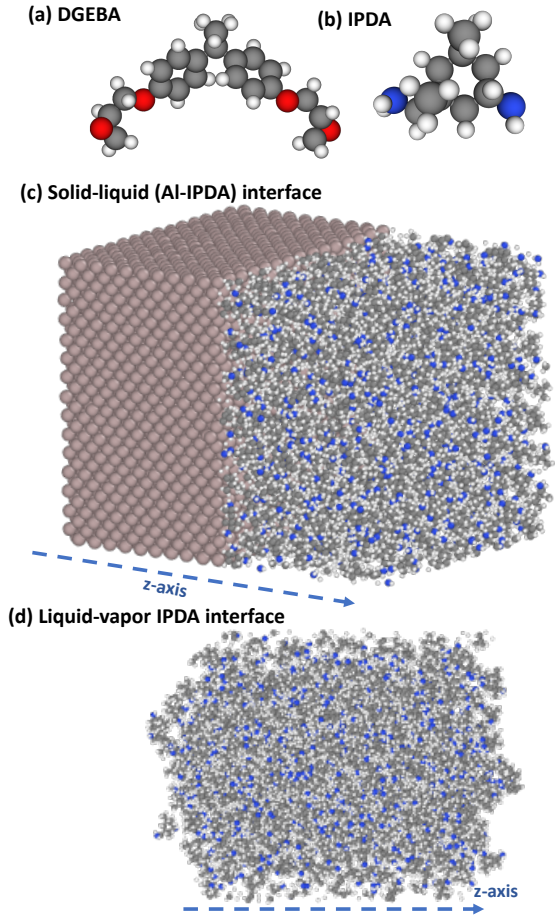

FIG. 1. Molecular representations of a) the DGEBA epoxy monomer and b) the IPDA hardener; c) IPDA molecules interacting with an aluminum metal surface; d) slab of IPDA liquid in equilibrium with its vapor at 298 K. The z-axis is indicated for each geometry and corresponds to the axis perpendicular to the solid-liquid and liquid-vapor interfaces.

III. RESULTS AND DISCUSSION

A. Calculation of the work of adhesion

We start this section with a methodological aspect of the calculation by showing in Figure 2 the dependence of the work of adhesion on the number of windows and the total simulation time. These calculations were performed in the forward and backward directions to check the reversibility of the transformation along the reaction path for systems. Regardless of the number of windows (N_w = 20 or 40), Figure 2 shows that deviations on the work of adhesion between direct and reverse paths do not exceed 2 mJ m^{-2} over a total value of 299 mJ m^{-2}. This means that the amount of perturbation characterized by the value of $\Delta\lambda$ (0.05 or 0.025) between consecutive windows is adapted to provide the calculation of a reversible work. We observe in Figure 2 insignificant deviations between adhesion works calculated with 5, 20 and 40 ns. We use the set of simulations carried out with different input parameters to estimate a standard deviation of approximately 5 mJ m^{-2} which corresponds to a statistical uncertainty less than 2 % on this property. As a result, we take the route of applying 20 windows and 20 ns for the complete perturbation process.

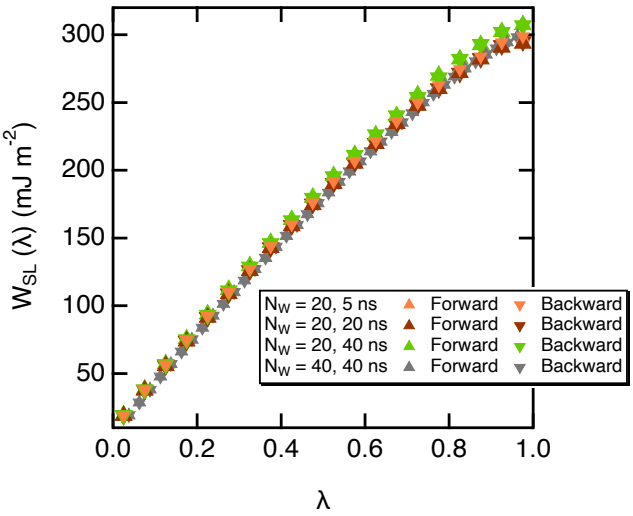

FIG. 2. Cumulative work of adhesion of IPDA molecules on an aluminum surface as a function of the coupling parameter λ for two numbers of windows (N_w= 20 and 40) and a total simulation time ranging from 5 to 40 ns. The value of the work of adhesion reads at $\lambda = 1$.

Subsequently, we first focus on the calculation of the work of adhesion of 300 molecules of water on an aluminum surface (5×5×5 units). The values reported in Figure 3a correspond to the averages performed over both directions. The result of this calculation is shown in Figure 3a with $\alpha = 1$ where α is defined in Eq.(26). In this case, the work of adhesion was found to be equal to (256 ± 1) mJ m^{-2}. By using Eq.(3), an experimental surface tension of water[53] of 72 mJ m^{-2} and a contact angle measured experimentally of 85°, we obtain an experimental work of adhesion of 78 mJ m^{-2} indicating that the simulated and experimental properties are by no means comparable. The large value obtained by simulation indicates that the cross interactions are too strong. An alternative to reproduce the experimental work of adhesion is to reduce the cross-interactions between the solid and liquid by introducing an α parameter less than or equal to 1, as expressed by the following equation:

$$\varepsilon_{SL} = \alpha\sqrt{\varepsilon_{SS}\,\varepsilon_{LL}} \qquad (26)$$

The works of adhesion are also shown in Figure 3a for different α values. As expected, we observe that the work of adhesion decreases from 256 to 4.1 mJ m^{-2} as the strength of the interactions between the solid and liquid decreases. It is then possible to reproduce the experimental work of adhesion by choosing $\alpha = 0.469$. This means that the cross-interactions must be significantly reduced by about 53 % to accurately predict the adhesion property of water on aluminum. This is not surprising, given the parameters of aluminum atoms[44] and water molecules[45] come from different force fields that have never been optimized together on this property.

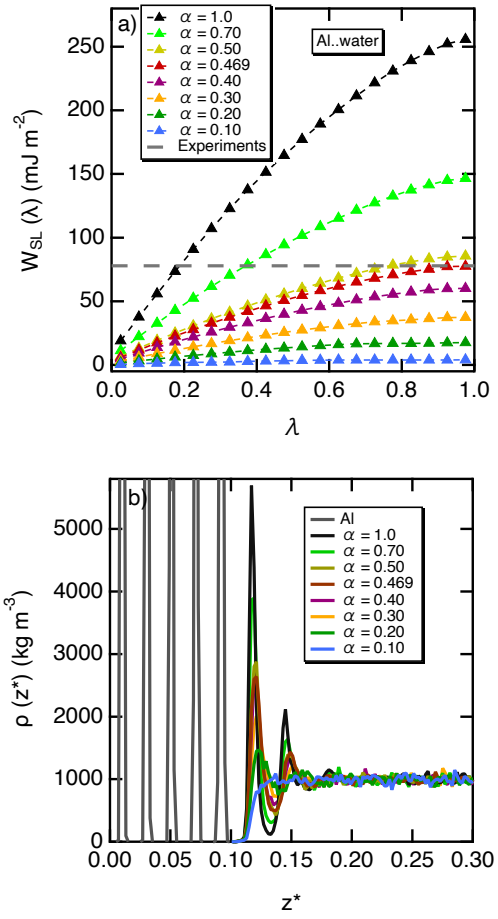

FIG. 3. a) Cumulative work of adhesion of water on an aluminum surface as a function of the coupling parameter for different cross-interactions between aluminum atoms and atoms of water molecules at 300 K; b) atomic density profiles along the normal direction to the metal surface as a function of the reduced z^*-position defined by $z^* = z/L_z$ where L_z is the box dimension of the simulation cell. The density profiles are shown for various values of α.

A microscopic view of the decrease of the cross-interactions between the metal and liquid can be observed on the density profiles of water molecules along the normal direction to the metal surface. These density profiles are shown in Figure 3b for decreasing interaction strength between metal and liquid. When the interaction is strongest ($\alpha = 1$), the density profile of water molecules show a well-pronounced peak of adsorption, followed by a second peak with a lower but still significant amplitude. These two peaks inform us about a strong structuring of water molecules close to the metal surface through the formation of two ordered layers. The amplitude of the peaks weakens with decreasing α-values. A value of $\alpha = 0.469$ leads to a good agreement between the experimental and simulated works of adhesion, without compromising the two well-ordered layers of water that results from an adaptation of the three-dimensional hydrogen-bond network of bulk conditions to a two-dimensional geometry imposed by the interaction with a surface[29]. In the case of the metal-water interaction, it is then possible to combine a good reproduction of the work of adhesion and the structure of water close to the metal surface.

We extend the study to the interaction of 40 molecules of DGEBA and 60 molecules of IPDA with the aluminum surface, so as to simulate about 2000 atoms of liquid. We proceeded likewise and report the works of adhesion in Figure 4a for DGEBA molecules and in Figure 4b for IPDA molecules. The experimental works of adhesion are calculated via Eq.(3) by considering the contact angles measured in this work. For the liquid-vapor surface tensions, the experimental values were not available and we replace them by the simulated ones.

The measured contact angles are respectively $\theta = 46°$ and $\theta = 36°$ for DGEBA and IPDA molecules. The corresponding work of adhesion are reported in Figure 4. We show again that the original cross-interactions parameters lead to a significant overestimation of the works of adhesion. For the interaction between DGEBA and the metal surface, we need to decrease the cross-interaction by about 58 % whereas a more drastic reduction of 73 % is required with IPDA to fit to the experimental property. The density profiles of Figure 4c show the local densities of DGEBA molecules in interaction with the aluminum surface. In the vicinity of the surface, we observe the adsorption is mainly characterized by only a single peak with a lower amplitude than that observed with water molecules. The same applies to IPDA molecules. This is due to the fact that these liquids are much less associated than water due to weaker interactions and a much less structured hydrogen bonding network. The reproduction of the experimental work of adhesion results in a decrease of the intensity of the peak of adsorption by 20 % whereas the vanishing of this peak requires weakening the cross-interactions by 80 % (see Figure 4c with $\alpha = 0.2$).

B. Calculation of the contact angle

The contact angle is determined during post-treatment of the MD trajectories by fitting a spherical cap to the water atomic density. The fit is performed using the max-

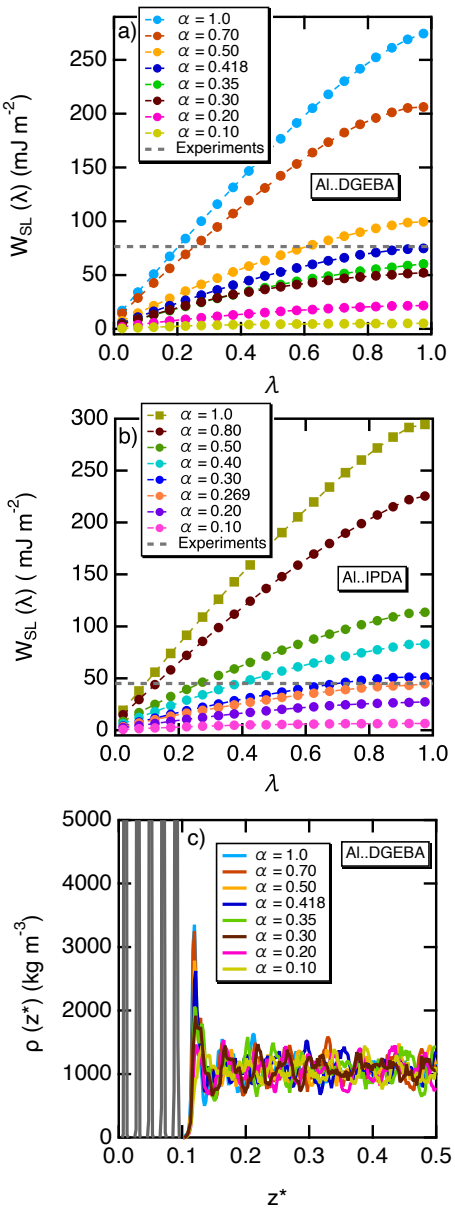

FIG. 4. Cumulative work of adhesion of a) DGEBA and b) IPDA on an aluminum surface as a function of the coupling parameter for different cross-interactions between aluminum atoms and atoms of the liquid phase at 300 K; c) atomic density profiles of the DGEBA molecules along the normal to the metal surface as a function of the reduced z-position. The density profiles are shown at different α values.

imum likelihood method. The log-likelihood to maximize is defined by

$$\mathcal{L} = \ln \prod_i \rho(\vec{r}_i) = \sum_i \ln \rho(\vec{r}_i) \tag{27}$$

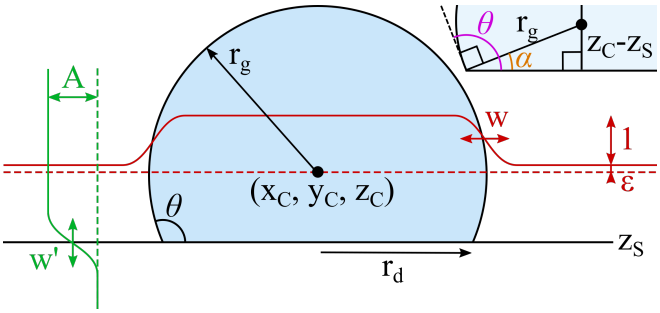

FIG. 5. Density profile used to determine the contact angle from simulation trajectories. The red curve is the density profile along the diameter of a spherical drop. The green curve is the density profile used to truncate the sphere. The functional definition of the full profile is given by Eq. (28).The angle θ is equal to $(90^\circ + \alpha)$ where $\sin\alpha = \frac{z_C - z_S}{r_g}$.

where the product and the sum run over all water atoms. The function ρ is chosen as

$$\rho = \left(\varepsilon + \frac{1}{1+\exp\left(r^2 - r_g^2\right)/w^2}\right)\left(\frac{A}{1+\exp\left(z_S - z\right)/w'}\right) \tag{28}$$

The notations are made explicit in Figure 5. The left bracket corresponds to a spherical profile whose section is drawn in red in Figure 5, where $\varepsilon \ll 1$ is the relative density in the vapor, r is the distance to the center of the drop (x_C, y_C, z_C), r_g is the drop curvature radius and w is the width of the liquid-vapor interface. The right bracket corresponds to a smooth step function which truncates the sphere and whose section is drawn in green in Figure 5, A is a normalization constant (not fitted) and z_S and w' are the position and the width of the solid-fluid interface. The contact angle and contact radius are then obtained by:

$$\theta = 90^\circ - \arcsin\left(\frac{z_S - z_C}{r_g}\right) \tag{29}$$

$$r_d = r_g \sin\theta \tag{30}$$

These values are averaged over all the frames of an MD trajectory.

The size dependence of microscopic droplets is described by the modified Young-Dupré equation[54–60]

$$\cos\theta = \cos\theta_\infty - \frac{\tau}{r_d\ \gamma_{LV}} \tag{31}$$

where θ is the contact angle of a nanodroplet simulated at the atomic scale, τ is the line tension and r_d is the radius of the contact surface between the nanodroplet and the material. θ_∞ is the equilibrium contact angle of a macroscopic angle corresponding to a droplet with r_d that tends to infinity. Simulations were performed for 4 ns on systems comprising 500, 1000, 2000, 5000, 10 000 and 25 000 molecules of water on a 80×80×10 supercell of aluminum (about 324 Å in the x and y directions).

TABLE II. Experimental values of work of adhesion (W_{SL}) calculated via Eq.(3). The contact angle (θ) was measured in this work and the simulated contact angle of water given in brackets is given for comparison. The surface tension (γ_{LV}) of water results from experiments[53] whereas the surface tensions of IPDA and DGEBA were calculated here by molecular simulations. The solid-vapor surface tension (γ_{SV}) was determined here by free energy perturbations. The solid-liquid surface tensions (γ_{SL}) were then deduced from Eq.(2).

W_{SL} (mJ m^{-2})	θ (°)	γ_{LV} (mJ m^{-2})	γ_{SV} (mJ m^{-2})	γ_{SL} (mJ m^{-2})
		Al..water		
78.0	84.6(81.0)	72.0	1161	1155
		Al..DGEBA		
76.7	44.4	41.8	1161	1126
		Al..IPDA		
45.1	33.2	24.5	1161	1140

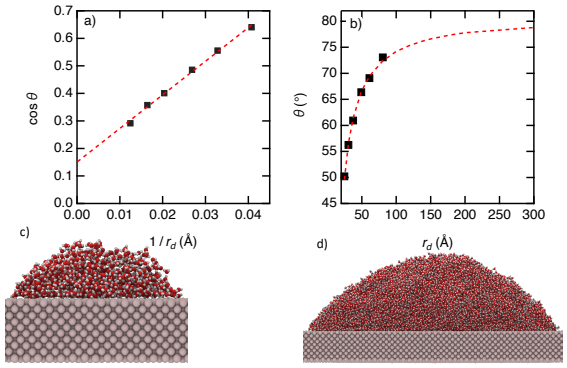

FIG. 6. a) Dependence of the cosine of the contact angle of water nanodroplets wetting an aluminum surface on the inverse of the radius of contact r_d.; b) dependence of the contact angle on r_d. The fits are shown in red broken lines. The macroscopic contact angle θ_∞ was calculated by extrapolating $\cos\theta$ to $(1/r_d = 0)$ in part a); snapshots of water nanodroplets formed by c) 1000 and d) 25 000 water molecules.

Figure 6a shows the values of $\cos\theta$ as a function of $1/r_d$ for different nanodroplets of water wetting an aluminum surface. The cross-interaction between water molecules and the aluminum surface were calculated with $\alpha = 0.469$ to match the experimental work of adhesion. Figure 6b shows the same relationship but in a different form. First, we find that $\cos\theta$ decreases as the water nanodroplet size increases. The linear fit shown in Figure 6a confirms the agreement of our data with the Young's equation. Second, we observe that the simulated droplets show contact angles smaller to that of the macroscopic drop in line with a negative line tension τ. The linear regression yields a negative line tension τ of -9.1×10^{-11} J m^{-1} and a value of $\theta_\infty = 81°$ that agrees very well with the experimental value of 85°. We also reproduce very well the magnitude of τ which is of the order of 10^{-11} even if there are still many controversies about the sign of the line tension[58–61]. Typical configurations of nanodroplets are given in parts c) and d) of Figure 6.

C. Liquid-vapor surface tension

We report here the surface tensions of both constituents of the DGEBA-IPDA epoxy resin, with respectively simulating 400 and 600 molecules. We also report the surface tension of a mixture of these constituents (400 molecules of DGEBA and 200 of IPDA). The calculation was carried by using Eq.(16). Figure 7 shows the differences between the normal and tangential pressures profiles of DGEBA and IPDA at two temperatures. The components of the pressure tensor are the same in the bulk liquid and vapor phases, with a few more oscillations around zero in the condensed phase. The two peaks are symmetric, and each peak contributes equally to $\gamma(z)$. We also check that the bulk phases make no contribution to the local surface tension. The profiles of the components of the pressure tensor and of the local surface tension indicates that the simulated liquid-vapor systems with planar interfaces are in mechanical equilibrium.

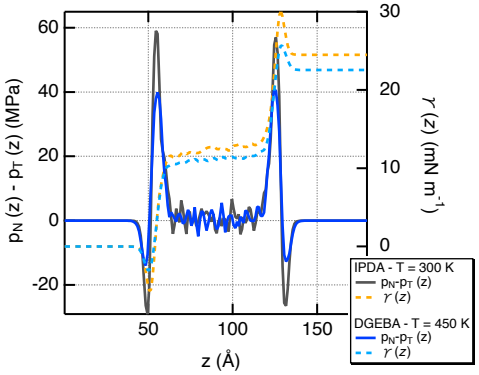

FIG. 7. Difference between the local normal $p_N(z)$ and tangential $p_T(z)$ components of the pressure tensor as a function of z calculated in the liquid-vapor interfaces of IPDA at 300 K and DGEBA at 450 K (left axis). The surface tension profile calculated with Eq.(16) is also shown for both molecules (right-axis).

Figure 8 shows that the surface tensions of DGEBA are higher than those of IPDA resulting in stronger intermolecular interactions for DGEBA in the liquid phase. This is in line with their respective density, which are of 1.17 g cm^{-3} for DGEBA and 0.92 g cm^{-3} for IPDA. The intermolecular interactions are stronger for DGEBA due to its aromaticity. We did not calculate the surface tension of water, since the calculation of its surface tension has been extensively studied with an accurate reproduction of the experimental property over a wide range of temperatures[5,62–65].

We now pay attention to the temperature dependence

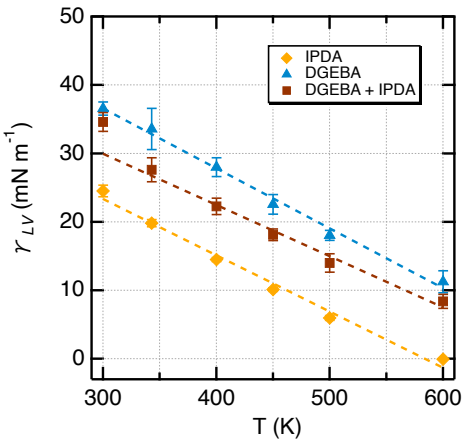

FIG. 8. Surface tensions of IPDA and DGEBA molecules as a function of the temperature. The error-bars were calculated by using block-averages on five independent simulations. The dotted lines represent the linear fit of the simulated values. For DGEBA and the DGEBA/IPDA epoxy mixture (2:1), the linear fits were performed by excluding the value at $T = 300\,\mathrm{K}$.

of the surface tension of DGEBA and IPDA systems. We observe that the temperature dependence of the surface tension is linear for IPDA and DGEBA with slopes of -0.08 ± 0.01 and $-0.09 \pm 0.01\,\mathrm{mJ\,m^{-2}\,K^{-1}}$, respectively. For the DGEBA/IPDA epoxy mixture with a 2:1 mixing ratio, the slope was estimated to be equal to -0.075 ± 0.005 by excluding the value at 300 K that deviates from the linearity. These values of slopes match very well with those found in liquids and molten polymers[66].

D. Solid-vapor surface tension

In a first step, the surface tension γ_{SV} was estimated by using the energy difference between the initial and final states of the cleavage process and neglecting the entropic contribution (Eq (20)). We considered a simulation cell formed by 49 000 aluminum atoms with $L_x = L_y = 141.61\,\text{Å}$ and $L_z = 120\,\text{Å}$. The average energy of the unified structure E_{U} is equal to $-6\,327\,179\,\mathrm{kJ\,mol^{-1}}$ and that of the separated structure $E_{\mathrm{S}} = -6\,027\,946\,\mathrm{kJ\,mol^{-1}}$ leading to a solid-vapor surface tension γ_{SV} of $1239\,\mathrm{mJ\,m^{-2}}$. The corresponding experimental surface tension[67] was found to be equal to $1180\,\mathrm{mJ\,m^{-2}}$.

We now apply the concept of perturbation and integration thermodynamics to mimic progressively the cleavage process from $\lambda = 0$ to $\lambda = 1$. However, the relatively strong value of γ_{SV} requires to increase significantly the number of windows to respect the reversibility between successive steps. We then apply 200 windows to calculate γ_{SV} by using the FEP formalism. We also introduce the calculation of this property by applying the TI definition to check the accuracy of both methods. The results are shown in Figure 9a in the forward and backward direction for the FEP method. For the TI method, we give only the average on both directions. W_{SV} is equal to 2322 and $2325\,\mathrm{mJ\,m^{-2}}$ in the forward and backward directions respectively, whereas TI provides values of 2322 and $2323\,\mathrm{mJ\,m^{-2}}$ for direct and reverse directions, respectively. We obtain an excellent agreement between both directions and methods, indicating that the number of windows and simulation time are adapted to the calculation of the solid-vapor surface tension of aluminum atoms. The values of γ_{SV} are then 1162 and $1161\,\mathrm{mJ\,m^{-2}}$ for FEP and TI methodologies and are in a perfect agreement with experiments[67] with a deviation less of 2 %. The comparison with the method using the difference in energy would show an entropy term $T\Delta S$ of about $78\,\mathrm{mJ\,m^{-2}}$ at $T = 300\,\mathrm{K}$

We now pay attention to the entropic term. It is possible to have an estimation of this property by considering the melting entropy of aluminum[68] $T\,\Delta S^{o}_{\mathrm{melting}} = T\,\frac{\Delta H^{o}_{\mathrm{melting}}}{T_{\mathrm{melting}}} = 11.6\,\mathrm{J\,mol^{-1}}$ where $T_{\mathrm{melting}} = 933\,\mathrm{K}$ and $T = 300\,\mathrm{K}$. By considering that only the first layer of atoms (400 atoms) of the metal surface ($\mathcal{A} = 40.46 \times 40.46\,\text{Å}^2$) is perturbed by the melting at the atomic level by increasing translational degrees of freedom, the entropic contribution to the solid-vapor surface tension would be about $69\,\mathrm{mJ\,m^{-2}}$.

By using Eq.(32), it is possible to calculate the entropic contribution by doing free energy calculations at different temperatures. We have calculated W_{SV} at 290 and 310 K and reported the values in Figure 9b with the FEP and TI techniques.

$$T\,\Delta S = -T\left(\frac{\partial \Delta G}{\partial T}\right) \approx -T\left(\frac{\Delta W_{\mathrm{SV}}}{\Delta T}\right) \qquad (32)$$

The choice of the temperature range is dictated by a significant response to the perturbation and the fact that the heat capacity of the metal is constant over this interval. We take $\Delta T = 20\,\mathrm{K}$. The values of the surface free energies are given in Figure 9b and differ by about $8\,\mathrm{mJ\,m^{-2}}$ over this temperature range.

We find that $T\Delta S$ is equal to 59 and $62\,\mathrm{mJ\,m^{-2}}$ for FEP and TI formalism. These calculated values confirm the order of magnitude of the previous estimates. We show here that both FEP and TI methods are able to provide the solid-vapor surface tension by doing no approximation on the entropic term. Figure 9c shows the values of the solid-vapor surface tensions of the aluminum surface at two different temperatures. The value of γ_{SV} calculated from the energy difference at 450 K shows an unexpected increase of the interfacial property with the temperature whereas the method considering the entropy in the calculation exhibits a decrease of γ_{SV} with increasing temperature. We estimate the entropy contribution $T\Delta S$ to be equal to $171\,\mathrm{mJ\,m^{-2}}$ at 450 K. The variation of entropy in the range of 300..450 K is larger than that of the energy (see Figure 9c) and therefore explains

the inversion of the trend of γ_{SV} with temperature. We conclude that only the method based on the calculation of the free energy can be used to predict this interfacial property at high temperatures at which neglecting the entropic term is no longer valid.

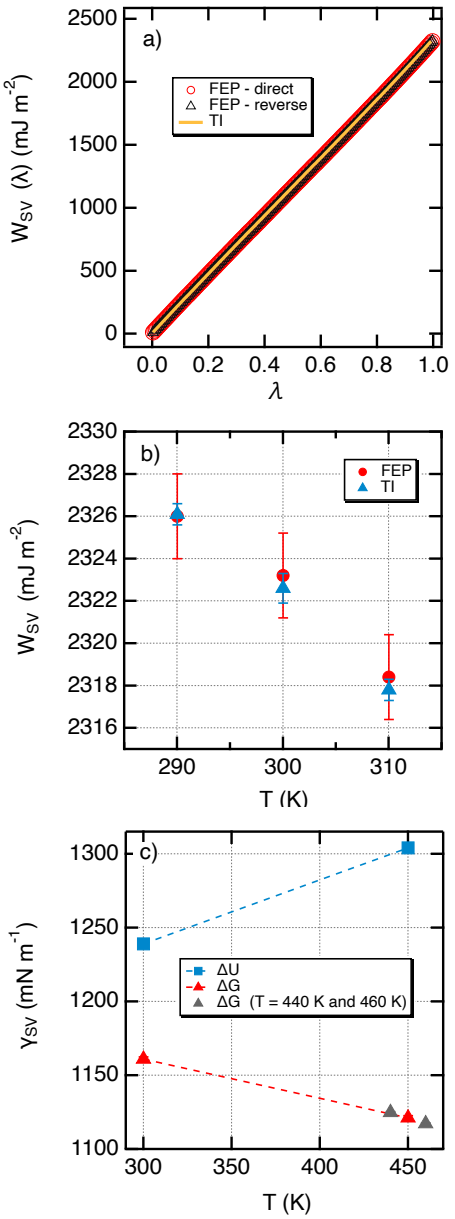

FIG. 9. a) Cumulative surface energy of aluminum metal surface calculated at 300 K by using the FEP and TI methods. For the FEP method, the values are given in the direct and reverse directions. For the TI method, we average the values in both directions. Calculations were performed over 200 windows; b) surface energy values calculated with FEP and TI at 290, 300 and 310 K and c) solid-vapor surface tensions at 300 and 450 K calculated by using the energy difference (ΔU) and the Gibbs free energy (ΔG) methods. The points calculated at 440 K and 460 K were used to calculate the entropy at 450 K .

E. Solid-liquid surface tension

The solid-liquid surface tension γ_{SL} can be calculated by an indirect way by using the definition of the work of adhesion as follows

$$\gamma_{SL} = \gamma_{LV} + \gamma_{SV} - W_{SL} \tag{33}$$

This calculation avoids using the mechanical definition of the interfacial tension and considering the relationship between γ_{SL} and the elastic strain tensor (see Eq.(4)). The values of the solid-liquid interfacial tensions are given in Table II for water, DGEBA and IPDA liquids interacting with the aluminum surface. We establish here that the calculation of W_{SL} and γ_{SV} are under control through perturbation and integration thermodynamic methods. The calculation of γ_{LV} is also under control through the mechanical definition of the surface tension, provided that the molecular models are well transferable to this property. It results that Eq.(33) represents an accurate way of calculating γ_{SL}. Since the values of γ_{LV} and W_{SL} are small compared to γ_{SV}, the value of γ_{SL} is imposed by γ_{SV} and we find values ranging 1126 to 1155 mJ m^{-2} for the interaction of water, DGEBA and IPDA with an aluminium surface. These strong γ_{SL} values indicate that the interface between these liquids and the aluminium atoms of the surface is highly ordered and not very fluid.

IV. CONCLUSION

We report molecular simulations of the interaction between liquids and an aluminum metal surface. Some key-properties for understanding and characterizing the solid-liquid interface are the work of adhesion and the contact angle. The primary objective of this work was not to reproduce the experimental work of adhesion as we are aware that this property depends on the transferability of the molecular models but rather to show that the calculation of the Gibbs free energy performs very well in line with the calculations of contact angle and interfacial tensions. It is then possible to characterize the adhesion process through the different interfacial tensions.

We applied the methodology of the perturbation thermodynamic to calculate the work of adhesion of water, DGEBA and IPDA on an aluminum surface. Since the molecular models of these molecules were developed independently of those of the metal atoms, the cross-interactions between liquid and metal atoms were not expected to reproduce the experimental work of adhesion. Indeed, we showed here that these cross-interactions should be weakened by a factor α ranging from 0.47 to 0.27 depending on the liquid studied. The analysis of the molecular density profiles along the direction normal to the surface confirms a layering of molecules at the interface of metal atoms. By using these modified cross-

interactions, we demonstrated that it is possible to calculate the contact angle of water molecules interacting with the aluminum surface by considering the size-dependence of the nanodroplet.

We extended the study to the calculation of the liquid-vapor surface tension of DGEBA and IPDA at different temperatures. We also investigated a 2:1 DGEBA/IPDA mixture. These simulations reproduce the fact that the surface tensions of DGEBA are greater than those of IPDA in agreement with their densities. We also calculated the slope of the temperature dependence of the surface tension for these systems, which were found to match with the slopes of many liquids and molten polymers.

We completed the study of the solid-liquid interface by the calculation of the surface free energy of aluminum by using the perturbation and integration thermodynamics approaches. The simulations showed an excellent agreement with experiments and also the ability of calculating the entropy contribution. This approach performed successfully for the calculation of the solid-vapor interfacial tension. We showed that it was possible to deduce the solid-liquid interfacial tension without needing to consider the components of the elastic strain tensor through a mechanical definition of the interfacial tension.

The methodologies described in this paper opens promising perspectives since they will help us in characterizing the solid-liquid interface through all its contributions γ_{SL}, γ_{SV} and γ_{LV}. The knowledge of the work of adhesion and its different contributions is fundamental to test the validity of molecular force-fields used for the modelling of adsorption processes. A possible extension of this work could be the calculation of the percolation threshold in polymer composites filled with conductive metal particles by using mesoscopic models. This interfacial property can thus be used to develop realistic and accurate coarse-grained force-fields needed to represent the polymer composites with a representative system-size.

ACKNOWLEDGMENTS

MO, ABM and CL would like to thank all the members of SimatLab for stimulating discussions about this work. SimatLab is a joint public-private laboratory dedicated to the multi-scale modelling of polymer materials. This laboratory is supported by Michelin, Clermont Auvergne University (UCA), CHU of Clermont-Ferrand and CNRS. We are also grateful to the Mésocentre Clermont Auvergne University for providing computing and storage resources.

DATA AVAILABILITY

The data that support the findings of this study are available from the corresponding author upon reasonable request.

[1] T. Young, Philos. Trans. R. Soc. London **95**, 65 (1805).
[2] A. Marmur, Soft Matter **2**, 12 (2006).
[3] E. Bormashenko, Low Temperature Physics **42**, 622 (2016).
[4] J. N. Israelachvili, *Intermolecular and surfaces forces*, 3rd ed. (Academic Press, New-York, 2011).
[5] A. Ghoufi, P. Malfreyt, and D. J. Tildesley, Chem. Soc. Rev. **45**, 1387 (2016).
[6] M. P. Allen and D. J. Tildesley, *Computer Simulation of Liquids : Second Edition* (Oxford: Clarendon Press, 2017).
[7] J. S. Rowlinson and B. Widom, *Molecular Theory of Capillarity* (Clarendon Press, Oxford, 1982).
[8] J. K. Lee, J. A. Barker, and G. M. Pound, J. Chem. Phys. **60**, 1976 (1974).
[9] K. S. Liu, J. Chem. Phys. **60**, 4226 (1974).
[10] A. Trokhymchuk and J. Alejandre, J. Chem. Phys. **111**, 8510 (1999).
[11] F. Goujon, P. Malfreyt, A. Boutin, and A. H. Fuchs, Mol. Simul. **27**, 99 (2001).
[12] C. Ibergay, A. Ghoufi, F. Goujon, P. Ungerer, A. Boutin, B. Rousseau, and P. Malfreyt, Phys. Rev. E **75**, 051602 (2007).
[13] F. Goujon, A. Ghoufi, P. Malfreyt, and D. J. Tildesley, J. Chem. Theory Comput. **11**, 4575 (2015).
[14] G. J. Gloor, G. Jackson, F. J. Blas, and E. de Miguel, J. Chem. Phys. **123**, 134703 (2005).
[15] F. Biscay, A. Ghoufi, F. Goujon, V. Lachet, and P. Malfreyt, J. Chem. Phys. **130**, 184710 (2009).
[16] R. Shuttleworth, Proc. Phys. Soc. A **63**, 444 (1950).
[17] P. Müller and A. Saul, Surf. Sci. Rep. **54**, 157 (2004).
[18] A. Kaarma, Phys. Rev. E **48**, 3441 (1993).
[19] F. Leroy, D. J. V. A. dos Santos, and F. Müller-Plathe, Macromol. Rapid. Commun. **30**, 864 (2009).
[20] F. Leroy and F. Müller-Plathe, J. Chem Phys. **133**, 044110 (2010).
[21] F. Leroy, S. Liu, and J. Zhang, J. Phys. Chem. C **119**, 28470 (2015).
[22] F. Leroy and F. Müller-Plathe, Langmuir **31**, 8335 (2015).
[23] A. R. Nair and S. P. Sathian, J. Chem Phys. **137**, 084702 (2012).
[24] B. B. Laird, R. L. Davidchack, Y. Yang, and M. Asta, J. Chem. Phys. **131**, 114110 (2009).
[25] H. D. d'Oliveira, X. Davoy, E. Arche, P. Malfreyt, and A. Ghoufi, J. Chem. Phys **146**, 214112 (2017).
[26] T. Dreher, C. Lemarchand, L. Soulard, E. Bourasseau, P. Malfreyt, and N. Pineau, J. Chem. Phys. **148**, 034702 (2018).
[27] T. Dreher, C. Lemarchand, N. Pineau, E. Bourasseau, A. Ghoufi, and P. Malfreyt, J. Chem Phys. **150**, 014703 (2019).
[28] A. Ghoufi and P. Malfreyt, Mol. Phys. **119**, e1948121 (2021).
[29] F. Goujon, A. Ghoufi, and P. Malfreyt, J. Chem Phys. **154**, 104504 (2021).
[30] C. D. van Engers, N. E. A. Cousens, V. Babenko, J. Britton, B. Zappone, N. Grobert, and S. Perkin, Nano Lett. **17**, 3815 (2017).
[31] J.-P. Pascault and R. J. J. Williams, General concepts about epoxy polymers, in *Epoxy Polymers* (John Wiley & Sons, Ltd, 2010) Chap. 1, pp. 1–12.
[32] W. Zwanzig, J. Chem. Phys. **22**, 1420 (1954).
[33] M. Mezei and D. L. Beveridge, Ann. N. Y. Acad. Sci. **482**, 1 (1986).
[34] A. Ghoufi and P. Malfreyt, Mol. Phys. **104**, 2929 (2006).
[35] C. Chipot and A. Pohorille, *Free Energy Calculations : Theory and Applications in Chemistry and Biology*, Springer Series in Chemical Physics (Springer, Berlin, Heidelberg, New York, 2007).
[36] R. P. Misra and D. Blankschtein, J. Phys. Chem. C **121**, 28166 (2017).
[37] K. Vanommeslaeghe, E. Hatcher, C. Acharya, S. Kundu, S. Zhong, J. Shim, E. Darian, O. Guvench, P. Lopes, I. Vorobyov, and A. D. Mackerell, J Comput Chem **31**, 671 (2010).
[38] K. Vanommeslaeghe and A. D. MacKerell, J Chem Inf Model **52**, 3144 (2012).

[39]K. Vanommeslaeghe, E. P. Raman, and A. D. MacKerell, J Chem Inf Model **52**, 3155 (2012).
[40]S. Nosé, Mol Phys **52**, 255 (1984).
[41]S. Plimpton, J Comput Chem **117**, 1 (1995).
[42]P. Hirel, Comput. Phys. Commun. **197**, 212 (2015).
[43]D. R. Lide, G. Baysinger, S. Chemistry, L. I. Berger, R. N. Goldberg, and H. V. Kehiaian, in *CRC Handbook of Chemistry and Physics*, Internet Version 2005 (CRC Press, Boca Raton, FL, 2005).
[44]H. Heinz, R. A. Vaia, B. L. Farmer, and R. R. Naik, J. Phys. Chem **112**, 17281 (2008).
[45]Y. Wu, H. L. Tepper, and G. A. Voth, J. Chem. Phys. **124**, 024503 (2006).
[46]T. C. Beutler, A. E. Mark, R. C. van Schaik, P. R. Gerber, and W. F. van Gunsteren, Chem. Phys. Lett. **222**, 529 (1994).
[47]J. G. Kirkwood and F. P. Buff, J. Chem. Phys. **17**, 338 (1949).
[48]J. H. Irving and J. Kirkwood, J. Chem. Phys. **18**, 817 (1950).
[49]J. P. R. B. Walton, D. J. Tildesley, J. S. Rowlinson, and J. R. Henderson, Mol. Phys. **48**, 1357 (1983).
[50]J. P. R. B. Walton, D. J. Tildesley, J. S. Rowlinson, and J. R. Henderson, Mol. Phys. **50**, 1381 (1983).
[51]K. Shi, E. E. Santiso, and K. E. Gubbins, J. Chem. Phys. **154**, 084502 (2021).
[52]A. Harasima, *Advances in Chemical Physcis* (Wiley & Sons, 1958) pp. 203–237.
[53]G. Vasquez, E. Alvarez, and J. M. Navaza, J. Chem. Eng. Data **40**, 611 (1995).
[54]J. W. Gibbs, *The Collected Works of J. Willard Gibbs, Vol.1, Thermodynamics* (New Haven, Yale University Press, 1945).
[55]J. H. Weijs, A. Marchand, B. Andreotti, D. Lohse, and J. H. Snoeijer, Phys. Fluids **23**, 022001 (2011).
[56]L.-O. Heim and E. Bonaccurso, Langmuir **29**, 14147 (2013).
[57]C. Li, J. Huang, and Z. Li1, Sci. Rep. **6**, 26788 (2016).
[58]M. Kitabata, T. Taddese, and S. Okazaki, Langmuir **34**, 12214 (2018).
[59]J. Zhang, P. Wang, M. K. Borg, J. M. Reese, and D. Wen, Phys. Fluids **30**, 082003 (2018).
[60]J. Cordeiro and S. Desai, J. Micro. Nanomanuf. **5**, 031008 (2017).
[61]D. Quere, Nat. Mater. **3**, 79 (2004).
[62]J. Alejandre, D. J. Tildesley, and G. A. Chapela, J. Chem. Phys. **102**, 4574 (1995).
[63]A. Ghoufi, F. Goujon, V. Lachet, and P. Malfreyt, J. Chem. Phys. **128**, 154716 (2008).
[64]C. Vega and E. de Miguel, J. Chem. Phys. **126**, 154707 (2007).
[65]P. Malfreyt, Mol. Simul. **40**, 106 (2014).
[66]S. A. Page, J. C. Berg, and J. A. A. Manson, J. Adhesion Sci. Technol. **15**, 153 (2001).
[67]W. R. Tyson and W. A. Miller, Surf. Sci. **62**, 267 (1977).
[68] CRC Handbook of Chemistry and Physics, 84th Edition Edited by David R. Lide (National Institute of Standards and Technology) (CRC Press LLC : Boca Raton, 2003), 2616 pp.